Hybrid Plasmonic Metasurface as Enhanced Raman Hot-Spots for Pesticide Detection at Ultralow Concentrations

Yazan Bdour,[a] Graham Beaton,[b] Juan Gomez-Cruz,[a] Oscar Cabezuelo,[b] Kevin Stamplecoskie[b] and Carlos Escobedo*[a,b]

A surface-enhanced Raman scattering (SERS) active metasurface composed of metallic nanohole arrays and metallic nanoparticles is developed. The metasurface can operate in aqueous environments, achieves an enhancement factor of 1.83×10^9 for Rhodamine 6G, and enables the detection of malachite green at a concentation of 0.46 ppb.

Sensors are fundamental tools developed to detect, observe, and monitor objects and activities that otherwise would go unnoticed through natural senses. Photonics-based sensors are a subcategory of chemical sensors designed to interact with light, resulting in a detectable and trackable frequency or energy shift.[1] The Raman effect is commonly used in photonic sensors, and is described as the inelastic scattering between photons and a molecule, where the interaction involves an energy exchange, resulting in an energy-shift of the scattered photon based on the intrinsic vibrational energy of molecular bonds. Therefore, the Raman effect provides with a unique spectrum for a specific molecule.[2] Tailored metallic nano-structures enable SERS-active hot spots, enhancing the signal intensities by order of magnitudes, offering a solution to a rather weak Raman signal – a well-known Achilles heel in real-world sensing applications.[3] The SERS hot spots are the result of confinement of the electric field at the minuscule gaps within the nanostructures that give rise to electromagnetic enhancement of the Raman signal.[4] Recently, metamaterials have been investigated to generate SERS hot spots by metasurface-enhanced Raman scattering (mSERS), demonstrating a great potential for sensing applications.[5, 6] Metallic nanohole arrays (NHAs) are nanoplasmonic metasurfaces that have been used in SERS-based sensing.[7] Although NHAs can support SERS, the creation of hot spots via NHAs requires the separation distance between the nanoapertures to be extremely small in order to confine the electromagnetic field. Previous studies demonstrate SERS hot spot generation with pyramidal[8] and bowtie shaped metallic nanoholes.[9] Although these studies demonstrate NHAs could be compelling SERS substrates, nanofabrication of three dimensional structures is inherently challenging, expensive and difficult to adapt to large-scale production. However, NHAs that are produced with standard membrane technologies can be used in combination with other metallic nanostructures, such as nanoparticles (NPs), to enable SERS. Metallic NPs, in fact, can also generate SERS hot spots as colloids,[10] or deposited as films.[11, 12] More recently, hybrid metallic nanostructures, from the combination of subwavelength apertures and NPs are gaining interest, and theoretical studies demonstrate their plasmonic resonance potential,[13] and SERS generation.[14] Practical devices have been achieved by tapping NPs atop a closed-ended NHAs, creating an mSERS-active substrate.[15] Similar in design, Au NPs have been placed inside resonant dead-ended nanoapertures with a simple immersion step.[16] This approach has potential for generating the enhancement required for SERS, as supported by the simulations, but lacks the benefits of nanoconfinement within the plasmonic nanostructure that a flow-through format could provide.

Here, we present an mSERS-active hybrid structure through the assembly of metallic NPs onto metallic flow through NHAs, capable of signal enhancement, also referred to as extra SERS enhancement, in aqueous environments. The NPs are transported to the nanoapertures using electrokinetic forces, creating a unique metasurface that, when exposed to Raman laser, is able to enhance the signal by orders of magnitude due to the nanoscopic spacing between the nanostructures. With these hybrid nanostructures, a maximum enhancement of 1.83×10^9 with Rhodamine 6G (R6G) is achieved, similar in degree of enhancement compared to reported high performing SERS-active substrates,[17] and a magnitude greater with respect to high-performing reported NHA ($EF \approx 10^7$),[18] and NPs ($EF \approx 10^6$) substrates.[19] The added benefit with this hybrid nanostructures is the utilization of flow-through nanoholes, that allows for the free movement of NPs and analytes across the plasmonic structure. The ability to easily, efficiently and quickly observe SERS in aqueous environments without the use of biotags, highlights the potential of the hybrid nanostructure in SERS-based biosensing applications.

a. *Department of Chemical Engineering, Queen's University, 19 Division St, Kingston, ON K7L 3N6, Canada. E-mail: ce32@queensu.ca*

b. *Department of Chemistry, Queen's University, 90 Bader Lane, Kingston, Ontario, K7L 3N6, Canada.*
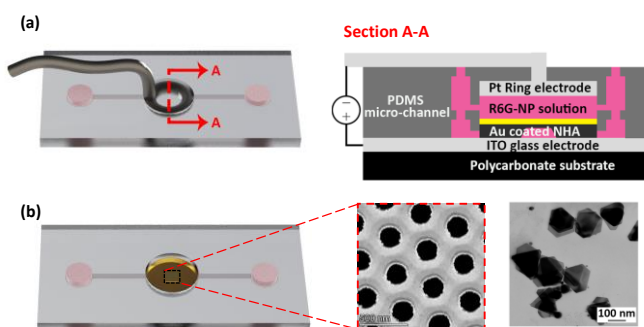
Figure 1. Schematic representation of the microfluidic chip assembly containing ring electrode, NHAs and solution with NPs. (a) Illustration of the top microfluidic layer containing the ring electrode, microchannel and central reservoir. (b) Illustration of the bottom microfluidic layer containing the hybrid metasurface indicating the location of the NHAs, the NP solution, the microchannel, and the central reservoir. Section A-A is the cross-sectional view of the illustration, displaying the complete assembly.

A polydimethyl(siloxane) (PDMS) microchannel chip used to assemble the hybrid NHA-NP structure is schematically illustrated in Fig. 1. The chip consists of two merged microfluidics chips, a top layer that contains a Pt ring-shaped wire electrode, and a microchannel that allows for the transport of R6G and NPs atop the NHAs (Fig 1a); and a bottom layer that contains a tight fitted NHA, as well as a microchannel, allowing for R6G and NPs transportation below the NHA (Fig 1b). When the two halves are combined, a central reservoir is created where the NHAs can combine with NPs, creating the hybrid surface, and directly obtain R6G Raman spectra. A cross-sectional view is shown in Fig. 1a, illustrating the assembly, and the position of each element to make the hybrid metasurface. The ring electrode rests approximately $500\ \mu m$ above the NHAs, allowing for unimpeded laser exposition, and direct Raman signal measurements. The Raman signal is acquired using an micro-ID Raman microscope (785 nm, 10.7 mW) system, while a DC voltage bias being applied spanning $-3.0\ V$ to $+3.0\ V$ at $0.2\ V$ increments through the electrodes. The NHAs are $200\ nm$ thick silicon nitride membrane containing $200\ nm$ diameter sized holes, with $400\ nm$ periodicity, spanning $500 \times 500\ \mu m^2$, coated with $100\ nm$ Au metallic film (additional details available in ESI). Two types of citrate-capped Ag triagonal, hexagonal, and truncated triagonal plates are synthesized and utilized for the hybrid surface: a) Nanoparticles 1 (NP1): 5 - 120 nm triagonal plates (mode of 35 nm) and b) Nanoparticles 2 (NP2): 10 - 100 nm (mode of 37 nm) (particle size distribution and additional details available in ESI).[20] These NPs were chosen due to their sizes and shapes, smaller than the diameter of nanoholes, which allows them to deposit at the rim of the nanoapertures. The shapes of the NPs is also an important factor in generating the SERS hot spots as the triagonal and hexagonal shapes have sharp corners, which induces a greater electromagnetic field enhancement at the SERS hot spots.[21]

SERS hot spots are the result of the electromagnetic enhancement by the confinement of the electric field lines at a specific area within a nanostructure. S-TEM images (Figs. S4-6, ESI; inset in Fig. 3) show the nanoparticles assembled on the rims of the NHAs after the application of the electric potentials. Hence, SERS can be achieved using hot spots enabled at the

gaps within the hybrid nanostructures. The surface aims to produce this gap to be between the NHAs and the NPs, which would lead to a significant signal enhancement in the assembly when compared to its individual components. To set the basis for comparison, the Raman spectrum of R6G on a 100 nm thin Au film is acquired as reference (Fig. S1, ESI). The thin Au film provides a baseline for the observed enhancement in the hybrid nansotructure, and for the calculation of the enhancement factor (EF) according to electromagnetic enhancement theory:[22]

$$EF = (I_{SERS}\ /\ I_{Raman}\ ) \times (N_{Raman}\ /\ N_{SERS}\ )$$

where I_{SERS}, and I_{Raman} are the intensities of SERS and normal Raman peaks of a wavenumber respectively. N_{SERS}, and N_{Raman} are the number of molecules contributing to the SERS and normal Raman signal respectively. N_{SERS} is estimated to equal $8.52 \times 10^{20}\ m^{-2}$ at the surface of the NHA, and N_{Raman} is calculated to equal $1.58 \times 10^{27}\ m^{-3}$ based on R6G density $(1.26\ g/cm^3)$. With a laser spot diameter of $15\ \mu m$, and penetration depth of $11\ \mu m$, the enhancement factor can be simplified to $EF = (I_{SERS}\ /\ I_{Raman}\ ) \times 20.45$.[23]

To highlight the Raman signal enhancement of the presented hybrid nanostructures, the R6G Raman spectra, and their corresponding EF, were obtained for each individual nanostructure (i.e. NHAs and NPs). Fig. 2 presents the normalized contour and intensity plots of the Raman spectra for NHAs (Fig. 2a), NP1 (Fig. 2b) and NP2 (Fig. 2c) on thin Au films at different applied electric potentials. The signal intensity for NHAs shows a significant increase when compared to Au thin film (Fig. S1, ESI), due to the capability of NHAs to produce SERS. Although slightly, the instensity increases with the applied potential, as shown by the coloured map, with a maximum EF of 1.02×10^7 at $1031\ cm^{-1}$. The enhancement vary across every applied potential, with average EF of 2.21×10^6 at the R6G bands (details in ESI). For NP1 at low voltages, where the colloidal NPs are still assumed to be suspended, the Raman signal is weak due to large separation distance between the particles within the colloidal suspension, preventing the generation of hot spots. In contrast, at higher voltages, the NP1-on-Au-film provides enhancement of the signal, in agreement with previous optoelectrofluidic SERS spectroscopy studies.[24] A key factor for the signal enhancement is the generation of hot spots from the gap between the film and the NPs, or between NPs [14, 25]. However, a higher EF is obtained with NP1, 1.43×10^7, at $1031\ cm^{-1}$ wavenumber, with an average EF 2.65×10^6 at the R6G bands across all applied potentials.
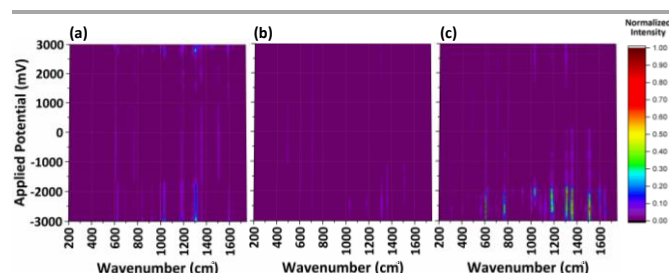

Figure 2. R6G Raman signal intensity plots employing (a) Au coated NHAs, (b) NP1 on thin Au film, and (c) NP2 on a thin Au film under applied electric potentials.

Similar results to NP1 are observed with NP2, but with a stronger Raman signal at higher voltages as there are slightly larger in size. The maximum EF observed with NP2 is 6.47×10^7 at $1031\ cm^{-1}$ wavenumber, and average EF of 1.15×10^7 at the R6G bands across all applied potentials levels. The SERS enhancement obtained from NHAs, NP1, and NP2, are comparatively lower than the current enhancement reported for SERS substrates.[17] Regardless, the individual hybrid metasurface components are able to produce SERS, which can be significantly enhhanced by the construction of a metasurface, through the combination of NHAs and NPs.

The SERS-active metasurface is formed when the periodic NHA is decorated with NPs, forming a unique subwavelength structure that interacts with the Raman laser photons to generate plasmonic hot spots. The distinctive feature of the metasurface is the flow-through array of subwavelength apertures that enable ionic migration and the nanofluidic transport of analytes and nanoparticles. The applied potential, in combination with the nanofluidic transport of the NHAs, are mechanisms used in manipulating the particles to approach the NHAs to create the minuscule gap needed for optimized SERS generation as numerical simulations demonstrate.[14, 15, 26] With these mechanisms, two hybrid metasurfaces are therefore created; one using NPs that are generally smaller (NP1) than the second one (NP2), to investigate the influence of the nanoparticle size in combination with the NHA. The Raman signals for both hybrid metasurfaces were formed and investigated by applying potentials ranging from 0 to $\pm\ 3\ V$. Fig. 3 presents the Raman intensity signals, as contour and color maps, of the hybrid nanostructures, i.e. the mSERS hot spots, generated from the combination of NP1 and NHA (Fig. 3a, b) and NP2 and NHA (Fig. 3c, d). The intensities in both cases are significantly higher compared to the individual components

(Fig. 2), and the enhancement of the Raman signal is consistent across a larger range of applied potential. The maximum EFs obtained with NP1-NHA metasurface, under positive and negative applied potential are, respectively, 1.83×10^9 and 1.17×10^5 at $1031\ cm^{-1}$, with an average EF of 3.26×10^8. The maximum enhancement obtained significantly overshadows the enhancement observed in Fig. 2, with a three order of magnitude extra SERS enhancement. Similarly, the NP2-NHA metasurface Raman spectra, presented in Fig. 3c and Fig. 3d, also display a consistent increase in signal intensity across the larger range of applied potential when compared to the individual nanostructures. The maximum EF obtained with NP2-NHA metasurface, under both positive and negative applied potentials, respectively, are 1.27×10^9 and 2.74×10^5 at $1031\ cm^{-1}$, with an average EF of 2.57×10^8. Therefore, this second hybrid nanostructure also provides with a three order of magnitude extra SERS enhancement compared to the individual nanostructures. In terms of Raman signal enhancement, both metasurfaces enable a similar enhancement factors with EF $\approx 10^9$, that can be used for high-performance SERS.[27, 28] The maximum extra SERS enhance-ments are observed under applied potentials between $+2.00\ V$ and $+2.80\ V$. At this potential range, the NPs do not aggregate and generate enhanced SERS hot spots along the nanohole rims. At relatively high potentials ($> \pm2.80\ V$) both metasurfaces show a significant reduction in the enhancement due to, presumably, excessive aggregation of NPs (Fig. S2, ESI), changing the topography of the surface. For applied potentials lower than $\pm1.40\ V$, the field does not contribute enough for the particles to approach the nanoholes, resulting in a less NP-populated surface and, consequently, a weaker enhancement, similar in magnitude to the individual nanostructures. Notably, negative applied potentials on the hybrid nanostructures result in enhancements of similar magnitude compared to NPs on the Au film. Comparatively, the NP1-NHA to NP2-NHA maximum and average extra SERS enhancement ratios are 1.33 and 2.39, respectively. The relatively small difference indicates that the resulting enhancement is not produced by the approximation or settling of the NPs within the vicinity of the nanoholes, but rather by the quantity and quality of hot spots generated.

The hybrid plasmonic metasurface was tested for the detection of Malachite Green (MG), a dye that is a banned pesticide, but still commonly used as antiparasitic drug in aquaculture
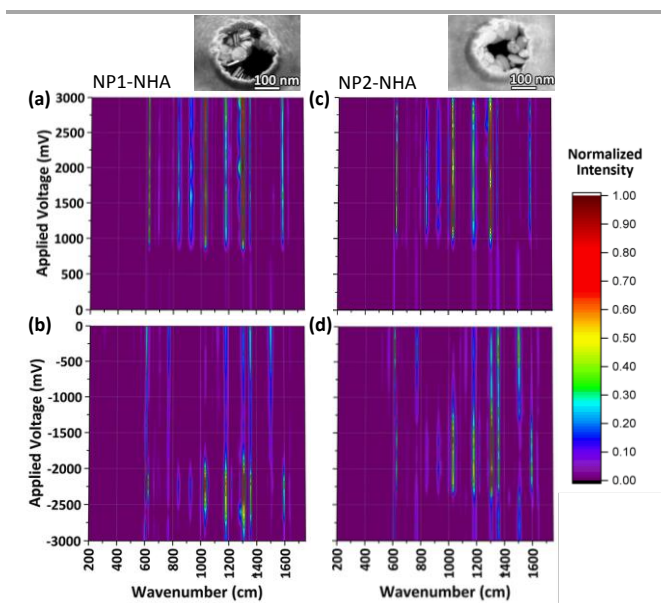

Figure 3. Raman signal intensities of R6G of the hybrid nanostructures based on (a) NP1 and an NHA, while under positive applied potential, and (b) NP1 and an NHA, while under negative applied potential. (c) NP2 and an NHA while under positive applied potential, and (d) NP2 and an NHA, while under negative applied potential. Top insets show S-TEM images of NP1 and NHAs (left) and NP2 and NHAs (right)
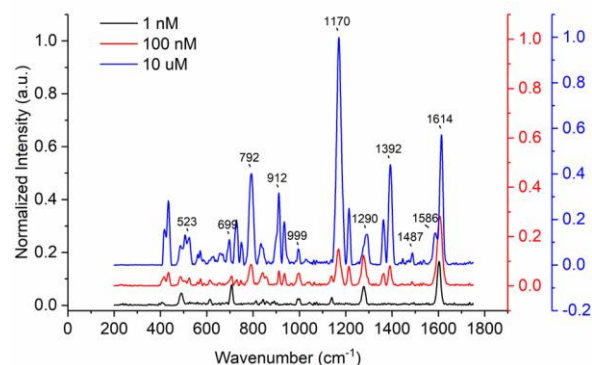

Figure 4. Normalized Raman spectra of MG at concentrations of 10 µM, 100 nM and 1 nM using the hybrid plasmonic metasurface, under an applied potential of 2 V.

products.[29] The best hybrid structure composition, comprising of NHAs and NP1 under 2 V, was used in this experiment at three different concentrations: 10 μM, 100 nM and 1 nM. The lowest concentration is equivalent to 0.4635 ppb, which can be considered an ultralow concentration in a real-world pesticed detection context. The Raman spectra of MG at the different concentrations are presented in Fig. 4. Even when the intensity is significantly reduced at 1 nM, the characteristic peaks at 523, 792, 912, 1290 and 1614 cm^{-1} are still clearly recognizable.[30] These results, collectively, demonstrate the capabilities of the hybrid plasmonic metasurface as sensor, which can be used for the detection of other anayltes of public and scientific interest.

In summary, we developed a hybrid flow-through metallic nanostructure that delivers extra SERS enhancement. The hybrid nanostructure is created by transposing metallic NPs onto metallic NHAs and is demonstrated as a hot-spot-enabled metasurface-enhanced Raman spectroscopy (mSERS) substrate. The resulting metasurface generated hot spots produced enhancement factors over 10^9 with the SERS prototype molecule R6G. The increased SERS enhancement provided by the hybrid nanostructure is orders of magnitude greater when compared to the individual nanostructures, i.e. NPs and NHAs, and is comparable, in magnitude, to recently published high-performing SERS substrates.[15] A unique aspect of the metasurface substrate is that it could achieve the enhancement without the use of any biotags, and within a complete aqueous environment in flow-through mode, facilitating nanoconfinement of target molecules within the nanostructure. The substrate has great potential for real-world sensing applications, as demonstrated for the detection of MG below the ppb limit and can be considered a plausible candidate for single-molecule SERS detection.

Conflicts of interest

There are no conflicts to declare.

Acknowledgements

Notes and references

Uncategorized References

1   Q. Duan, Y. Liu, S. Chang, H. Chen and J.-h. Chen, *Sensors*, 2021, **21**, 5262.
2   S. A. Maier, in *Plasmonics: Fundamentals and Applications*, Springer, 2007, pp. 21-37.
3   P. Karthick Kannan, P. Shankar, C. Blackman and C. H. Chung, *Advanced Materials*, 2019, **31**, 1803432.
4   S. Heeg, N. S. Mueller, S. Wasserroth, P. Kusch and S. Reich, *Journal of Raman Spectroscopy*, 2021, **52**, 310-322.
5   Y. Zeng, R. Ananth, T. J. Dill, A. Rodarte, M. J. Rozin, N. Bradshaw, E. R. Brown and A. R. Tao, *ACS Applied Materials & Interfaces*, 2022, **14**, 32598-32607.
6   Q. Zhang, L. Han, H. Jing, D. A. Blom, Y. Lin, H. L. Xin and H. Wang, *Acs Nano*, 2016, **10**, 2960-2974.
7   A. Prasad, J. Choi, Z. Jia, S. Park and M. R. Gartia, *Biosensors and Bioelectronics*, 2019, **130**, 185-203.
8   G. Palermo, M. Rippa, Y. Conti, A. Vestri, R. Castagna, G. Fusco, E. Suffredini, J. Zhou, J. Zyss and A. De Luca, *ACS applied materials & interfaces*, 2021, **13**, 43715-43725.
9   L. Jiao, P. Sun, Z. Xu, H. Feng, F. Xia, K. Zhang, W. Kong, L. Dong and M. Yun, *Optics Communications*, 2020, **474**, 126065.
10 Z. Ye, C. Li, Q. Chen, Y. Xu and S. E. Bell, *Nanoscale*, 2021, **13**, 5937-5953.
11 G. Beaton, Y. Bdour, C. Escobedo and K. Stamplecoskie, *ACS Applied Nano Materials*, 2022.
12 J. Huang, Y. Zhu, M. Lin, Q. Wang, L. Zhao, Y. Yang, K. X. Yao and Y. Han, *Journal of the American Chemical Society*, 2013, **135**, 8552-8561.
13 L. Wang, B. Xu, W. Bai, J. Zhang, L. Cai, H. Hu and G. Song, *Plasmonics*, 2012, **7**, 659-663.
14 J. Gomez-Cruz, Y. Bdour, K. Stamplecoskie and C. Escobedo, *Biosensors*, 2022, **12**, 128.
15 J. C. Ndukaife, Y. Xuan, A. G. A. Nnanna, A. V. Kildishev, V. M. Shalaev, S. T. Wereley and A. Boltasseva, *ACS nano*, 2018, **12**, 5376-5384.
16 J. Pillanagrovi and S. Dutta-Gupta, *Nanotechnology*, 2022, **33**, 485301.
17 A. I. Pérez-Jiménez, D. Lyu, Z. Lu, G. Liu and B. Ren, *Chemical science*, 2020, **11**, 4563-4577.
18 D. Lospinoso, A. Colombelli, M. Lomascolo, R. Rella and M. G. Manera, *Nanomaterials*, 2022, **12**, 380.
19 P. Liang, Q. Guo, T. Zhao, C.-Y. Wen, Z. Tian, Y. Shang, J. Xing, Y. Jiang and J. Zeng, *Analytical Chemistry*, 2022, **94**, 8466-8473.
20 K. G. Stamplecoskie and J. C. Scaiano, *Journal of the American Chemical Society*, 2010, **132**, 1825-1827.
21 B. J. Wiley, S. H. Im, Z.-Y. Li, J. McLellan, A. Siekkinen and Y. Xia, *Journal*, 2006, **110**, 15666-15675.
22 E. C. Le Ru and P. G. Etchegoin, *MRS bulletin*, 2013, **38**, 631-640.
23 K. Anju, R. Gayathri, P. Subha, K. R. Kumar and M. Jayaraj, *Microchemical Journal*, 2019, **147**, 349-355.
24 H. Hwang, D. Han, Y.-J. Oh, Y.-K. Cho, K.-H. Jeong and J.-K. Park, *Lab on a Chip*, 2011, **11**, 2518-2525.
25 G. Beaton, J. Zacks and K. Stamplecoskie, *Colloids and Surfaces A: Physicochemical and Engineering Aspects*, 2022, **646**, 128972.
26 Y. Pang and R. Gordon, *Nano letters*, 2011, **11**, 3763-3767.
27 O. Guselnikova, H. Lim, H. J. Kim, S. H. Kim, A. Gorbunova, M. Eguchi, P. Postnikov, T. Nakanishi, T. Asahi and J. Na, *Small*, 2022, **18**, 2107182.
28 C. Jin, Z. Du, C. Liu, F. Liu, J. Hu and M. Han, *Spectrochimica Acta Part A: Molecular and Biomolecular Spectroscopy*, 2022, **265**, 120372.
29 S. J. Culp and F. A. Beland, *Journal of the American College of Toxicology*, 1996, **15**, 219-238.
30 P. Kumar, R. Khosla, M. Soni, D. Deva and S. K. Sharma, *Sensors and Actuators B: Chemical*, 2017, **246**, 477-486.

Hybrid Plasmonic Metasurface as Enhanced Raman Hot-Spots for Pesticide Detection at Ultralow Concentrations

Yazan Bdour,[a] Graham Beaton,[b] Juan Gomez-Cruz,[a] Oscar Cabezuelo,[b] Kevin Stamplecoskie[b] and Carlos Escobedo[*a,b]

Materials and Methods

Nanohole Arrays

The metallic nanohole arrays (NHAs) were fabricated from PELCO holey 100-nm-thick silicon nitride membranes containing holes of 200 nm in diameter and 200 nm periodicity, spanning $500 \times 500 \ \mu m^2$ (Ted Pella, Redding, CA, USA). The membranes were coated with a thermally evaporated $5 \ nm$ layer of Cr, followed by 100 nm thick layer of Au using a 3 kW Linear e-gun physical vapour deposition evaporator (Thermionics, Hayward, CA) at Nanofabrication Kingston. The NHAs were optically inspected using an FEI-MLA Qunata 650 FEG-ESEM available at Queen's Facility for Isotope Research (Queen's University, Kingston, ON).

Experimental Setup

The chip assembly consists of two merged microfluidics chips that were designed using computer aided design software (SolidWorks, Dassault Systems) and 3D-printed using ANYCUBIC PHOTON S (Shenzhen, Guangdong, China). Sylgard 184 polydimethyl-siloxane (PDMS) (Dow Corning) mixed at 10:1 ratio, and baked at $70 \ ℃$ on a hot plate for 3 hrs was used to create the microchannels. The top layer was punched with a $1 \ mm$ biopsy tool to provide access to the Pt wire electrode. The bottom layer was punched with a $3 \ mm$ biopsy tool to securely host the NHAs. Rhodamine 6G (R6G) was purchased from Millipore Sigma (Oakville, ON, Canada). A 10-3 M R6G solution was pumped through the channels into the assembly using a $10 \ \mu L$ pipette.

Raman spectroscopy

All spectra were recorded using an Ocean Optics micro-ID Raman (785 nm, 10.5 mW) system equipped with a 40× objective. Spectra acquisition was conducted at 6 different locations over the NHAs, with an integration time of $5 \ s$. The spectra are averaged, and then normalized to the highest obtained peak.

R6G Raman Signal on Thin Au Film
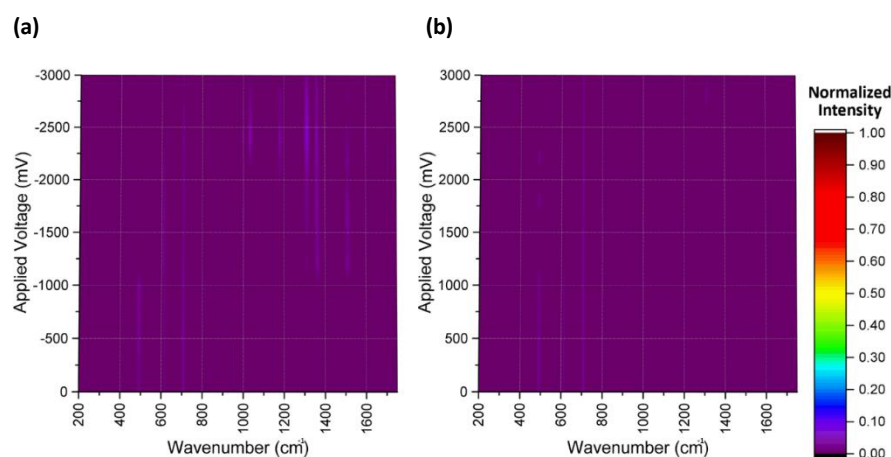
(a)   **(b)**

Figure SI 1. Normalized contour map of the Raman signal intensities of R6G on a thin Au film (a) under negative applied potential, (b) under positive applied potential.

Average Enhancement Factor

The enhancement factor requires an estimated value of the Raman laser penetration depth, which can be proportional to the laser spatial resolution, $\lambda/(NA)^2$. λ, is the wavelength of the illuminating light and NA is the numerical aperture. Typically for a Raman microscope, at 785 nm of laser light will penetrate 12 μm on a silicon wafer at ideal conditions.[1] However, due to the experimental setup, causing light scattering and focal length variance, leading to deformation within laser profile; thus reducing its penetration depth. A conservative estimate of the penetration factor is used of 11 μm rather than 12 μm, yielding a conservative enhancement factor of 20.45 rather than 22.31.

The enhancement factor is calculated at $623\ cm^{-1}$, $839\ cm^{-1}$, $925\ cm^{-1}$, $999\ cm^{-1}$, $1031\ cm^{-1}$, $1180\ cm^{-1}$, $1278\ cm^{-1}$, $1307\ cm^{-1}$, $1358\ cm^{-1}$, and $1596\ cm^{-1}$ wavenumbers. The maximum enhacement factor is found at $1031\ cm^{-1}$. The average enhancement factor is calculated by firstly averaging the enhancement factor of each wavenumber across all applied potentials, then averaging once again across all wavenumbers. Table SI 1 summarizes all average enhancement factors.

Wavenumber (cm^{-1})	Average Enhancement Factor				
	NHA	NP1-Au Film	NP2- Au Film	NP1-NHA	NP2-NHA
623	1.24E+06	7.77E+05	4.14E+06	1.05E+08	9.15E+07
839	1.12E+06	5.05E+05	1.05E+06	7.54E+07	6.72E+07
925	1.34E+06	4.69E+05	9.15E+05	1.49E+08	1.00E+08
999	1.38E+06	1.55E+06	2.94E+06	4.81E+07	5.60E+07
1031	2.21E+06	2.65E+06	1.15E+07	3.26E+08	2.57E+08
1180	1.92E+06	3.58E+05	1.01E+06	2.72E+07	2.83E+07
1278	1.77E+06	1.00E+06	3.25E+06	1.09E+08	3.28E+07
1307	1.81E+06	5.38E+05	1.53E+06	3.64E+07	2.97E+07
1358	2.30E+06	2.34E+05	5.65E+05	8.59E+06	5.42E+06
1596	3.86E+06	5.45E+05	1.64E+06	6.67E+07	4.86E+07
Average	1.90E+06	8.63E+05	2.86E+06	9.51E+07	7.16E+07

Table SI 1. Average EF of R6G obtained across different substrates.

NP deposition on NHA

Observed particle deposition, acquired using the Raman microscope, during experiments. The images indicate particle deposition in the vicinity of the NHAs upon the application of the electric potential, during data acquisition. At relatively high potentials ($> \pm 2.80\ V$), the particles were observed to aggregate at the surface of the Au thin film, as well as the NHAs.
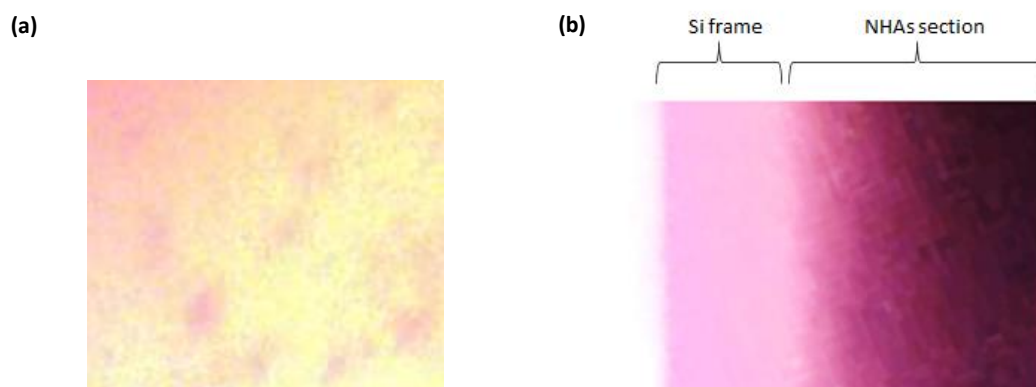

Figure SI 2. Microscope images obtained through the Raman lens of NP2 aggregation at $3.00\ V$ applied potential on (a) Au thin film and (b) NHAs.

Nanoparticles

For the synthesis of spherical silver nanoparticle seeds, solutions of 0.2 mM AgNO3 , 1 mM trisodium citrate and 0.2 mM Omnirad-2959 (photoinitator) were prepared. Upon excitation with UVA light, the photoinitator can undergo a Norish II cleavage to produce ketyl radicals capable of reducing Ag+ to Ag0. The solutions were combined and purged under N2 flow for ~30 minutes to remove oxygen quenching. The solution was irradiated under UVA light for ~10 minutes, until yellow in color, indicating the formation of spherical silver nanoparticles.

 These spherical seeds were then taken forward for photochemical shape control to generate the larger structures used for the SERS studies. 15 mL solutions containing 4.0 mM trisodium citrate and nanoparticle seeds were irradiated for 14 hours, open to atmosphere, with a Luzchem LED illuminator with varied excitation wavelengths. 625 nm and 825 nm light were used to generate the smaller and larger nanoparticle plates, respectively.

The nanoparticle size distribution measurements were carried out on Transmission electron microscopy (TEM) image analysis. The particles were imaged using a TALOS F200i transmission electron microscope operated at an acceleration voltage of 200 kV. The samples were prepared as an aqueous dispersion on a copper grid.

The TEM image study was done with ImageJ pixel measurements, where the distributions show a high size disparity for both nanoparticle dispersions. NP1 are composed of triangular and hexagonal plates, presented in Figure SI 3 (a). While NP2 share some of the shapes of NP1, but also include cylindrical ones, shown in Figure SI 3 (b). The TEM size distribution measurements determine a size of $35.77 \pm 1.21\ nm$ for NP1, and $37.38 \pm 3.07\ nm$ for NP2.
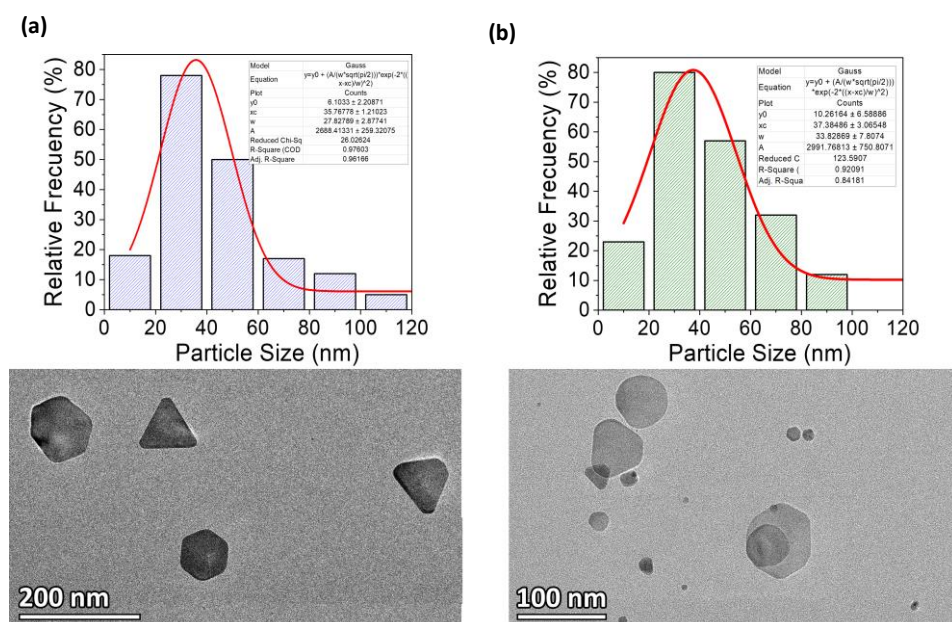
Figure SI 3. A bar graph presenting the size distribution and a TEM image of (a) NP1 (b) NP2.

SEM and TEM Imaging

The hybrid metastructures were observed under using scanning election microscopy (SEM) and scanning transmission electron microscopy (S-TEM). The SEM images were obtained using a Quanta 250 scanning election microscope operated at 20.0 kV, and the S-TEM images were acquired using the TALOS F200i transmission electron microscope operated at an acceleration voltage of 200 kV. Two separate samples were prepared as described in the experimental setup at 2.5 V applied potential using NP1 and NP2, respectively. Images from multiple devices used under different conditions were acquired. Representative images of the different devices and conditions are shown in the images below. A reference NHA platform unutilized in any experimental setup, or NP dispersions imaged using an SEM and S-TEM, is presented in Figure SI 4 (a) and SI 4 (b), respectively. Figure SI 5 shows a S-TEM image of a metasurface fabricated with NHA and NP1. In this image, the nanoparticles can be observed adjacent to the edge of the NHs, with their edges aligned to the rims. Similarly, a S-TEM image of a hybrid metasurface using NHA and NP2 is shown in Figure SI 6.
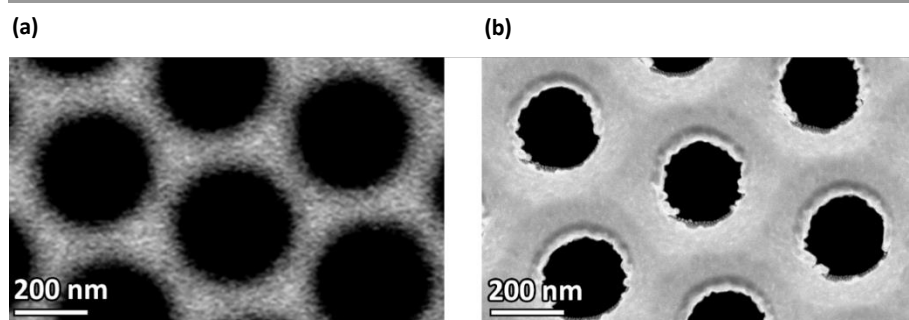

Figure SI 4. An unutilized NHA platform imaged under (a) SEM, and (b) S-TEM.
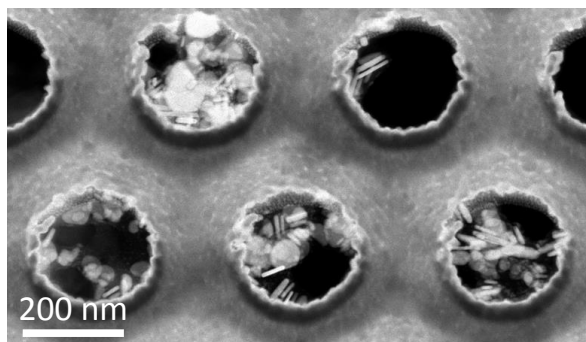
Figure SI 5. S-TEM image of nanoholes with assembled NP1 at an applied electric potential of 2.5 V.
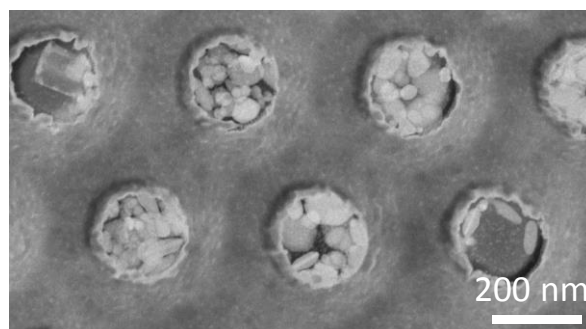

Figure SI 6. Three close-up S-TEM images of separate nanoholes decorated with NP2 at 2.5 V applied electric potential.

Repeatability and Reproducibility

Two new experiments were carried out to show the repeatability of the reproducibility of R6G peak enhancements on separate new devices. The measurements were carried out on 6 mapped locations on the NHAs as indicated in Figure SI 7. The R6G Raman spectra for new, independent devices is presented in Figure SI 8. The intensity of the Raman spectra is normalized to the peak intensities presented in the main manuscript.
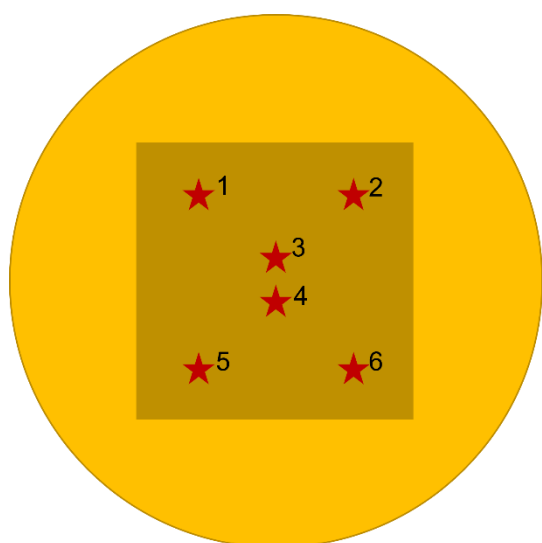

Figure SI 7. An illustration of an NHA-NP device indicating an approximate location of each spot the Raman spectra is acquired and mapped at various applied potentials.
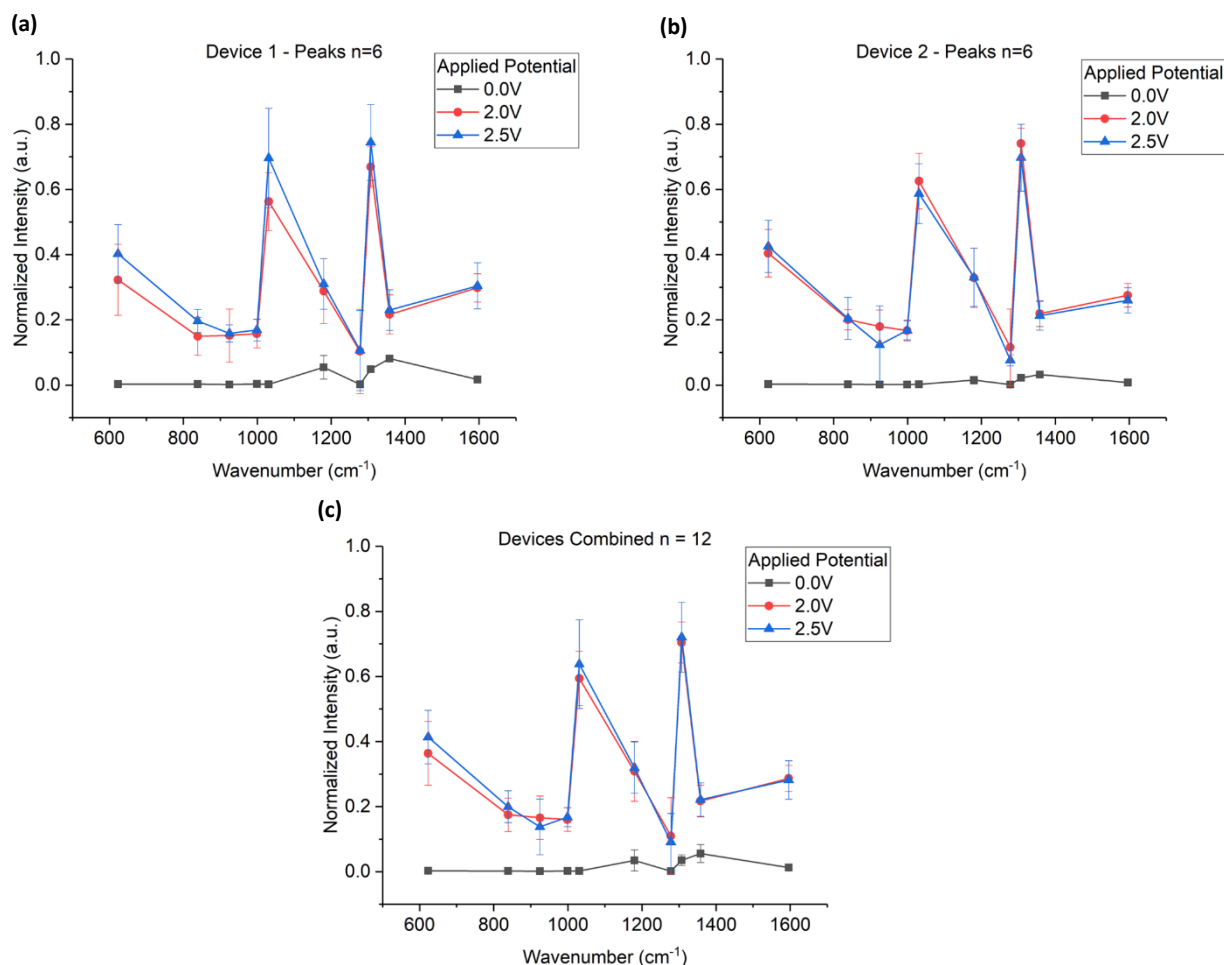
(a)

(b)

(c)

Figure SI 8. R6G normalized peaks intensity variability obtained from (a) Device 1, (b) Device 2 averaged out from 6 mapped out locations across the NHAs, highlighting the reproducibility and the repeatability of the enhancement. The variability from the devices in (c) are further compared when averaged out across the 12 spots from the combined devices.

Simulations

FDTD simulations were carried out on the structures to highlight the plasmonic response from each device. Nanohole array structures with dimensions of 200 nm diameter, 400 nm periodicity on 500 nm SiN2 and 50 nm Au, were simulated using an active region with a 4 nm mesh grid spacing. Prism shape nanoparticles with dimensions of 15 nm x 15 nm x 8 nm. Periodic boundary conditions (PBC) are used for the x and y axes boundaries to model the periodic nature of the NHAs, while perfect match layer (PML) boundary conditions are used in the z-direction to avoid light reflection from the propagation direction. The electromagnetic field was acquired through an observation area. The light source uses an input plane field with a y-axis polarized plane wave centered at 785 nm wavelength. The top view and 3D contour plots of the results are displayed in Figure SI 9 (a) and (b), respectively.

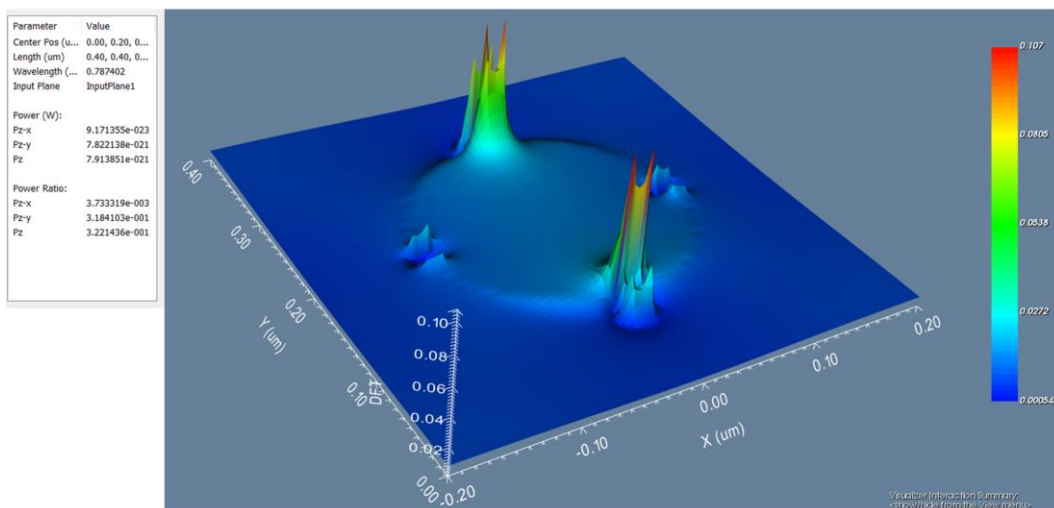Please do not adjust margins ChemComm

(a)
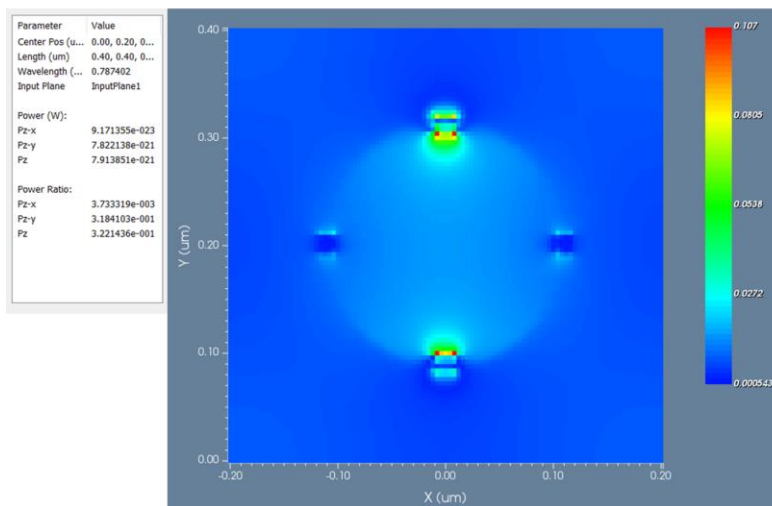
(b)

Figure SI 9. FDTD simulations showing (a) 2D top-view, (b) 3D contour plots of the plasmonic response of NPs on the rim of NH.

Malachite Green Raman Detection

Malachite Green oxalate salt (MG) was purchased from Millipore Sigma (Oakville, ON, Canada) and diluted to $10\ \mu M$, $100\ nM$, and $1\ nM$ concentrations. The spectra, presented in Figure SI 10, were recorded using an Ocean Optics micro-ID Raman (633 nm, 10.5 mW) system equipped with 40× objective. Each concentration was recorded on separate devices, where the average spectrum was obtained at 6 different locations across the NHAs across three different applied potentials, using $10\ s$ integration time. The spectra are averaged and normalized to the highest obtained peak.
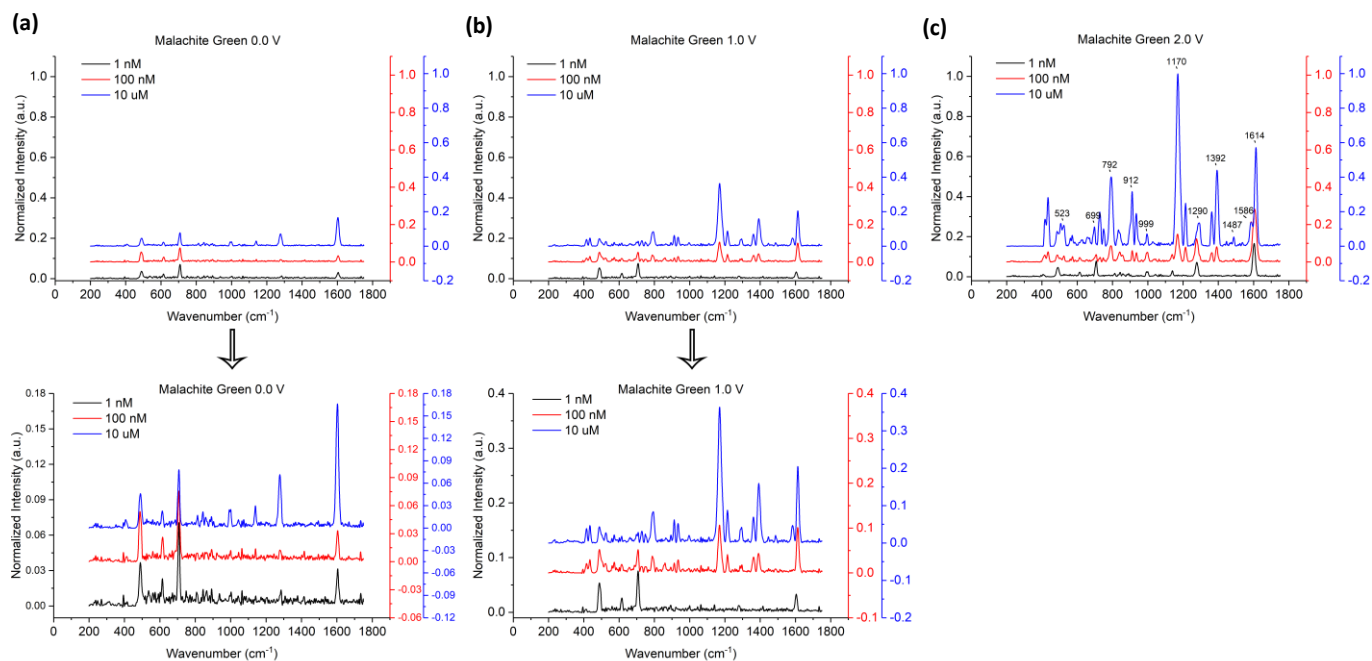
Please do not adjust margins

(a)

(b)

(c)

Figure SI 10. The normalized Raman spectra of MG observed at $10\ \mu M$, $100\ nM$, and $1\ nM$ concentrations under a) 0.0 V applied potential, b) 1.0 V applied potential, and c) 2.0 V applied potential.

Variable Instrument Conditions

The laser power of $\mathbf{10.5\ mV}$ and integration time of $\mathbf{5\ s}$ were chosen, as it was the best conditions to obtain the R6G Raman spectra without oversaturating the instrument. To highlight the oversaturation issues, Figure SI 11 presents R6G Raman spectra at the NHAs site under 2.0 V applied potential with different laser powers, and integration times.
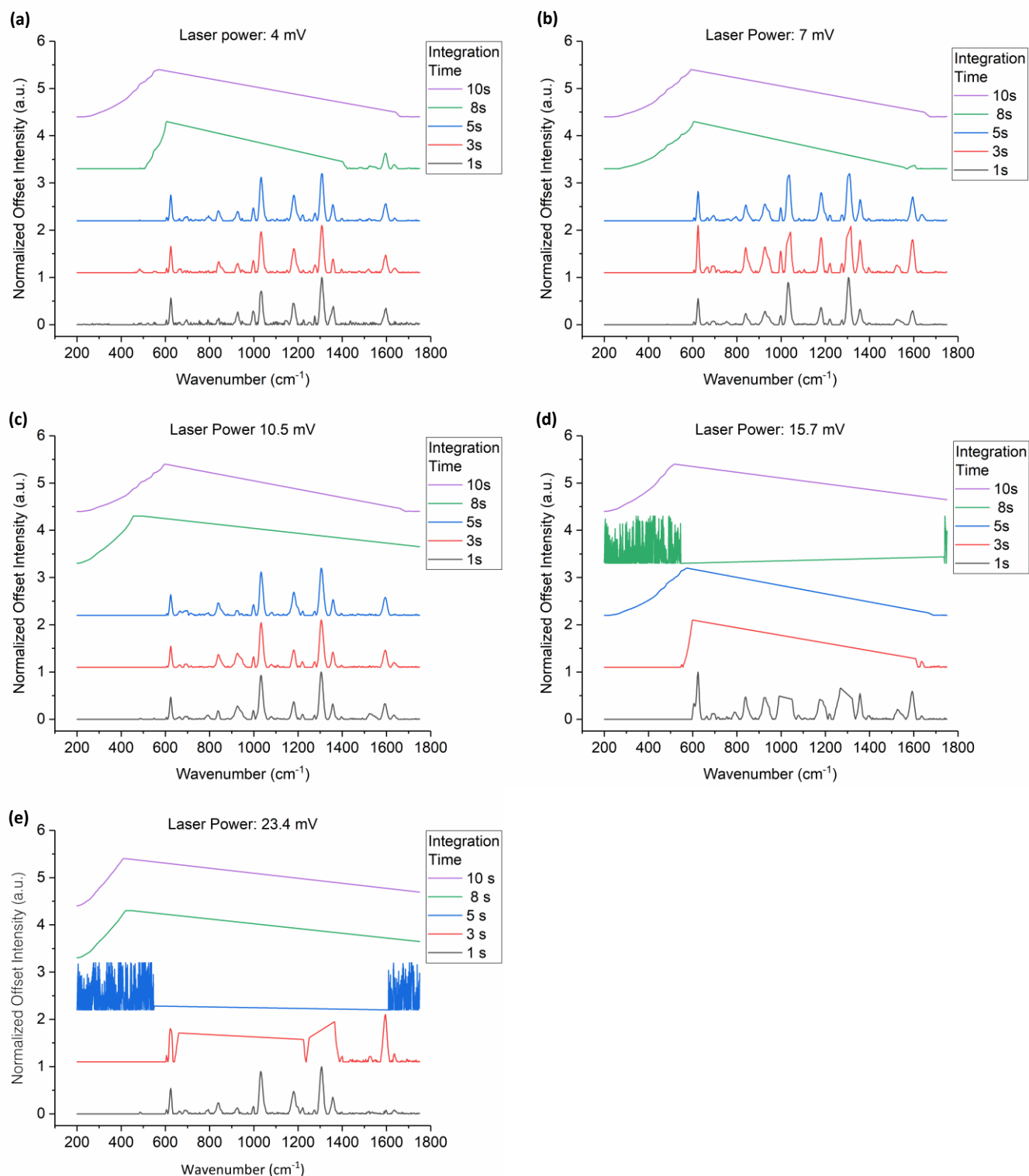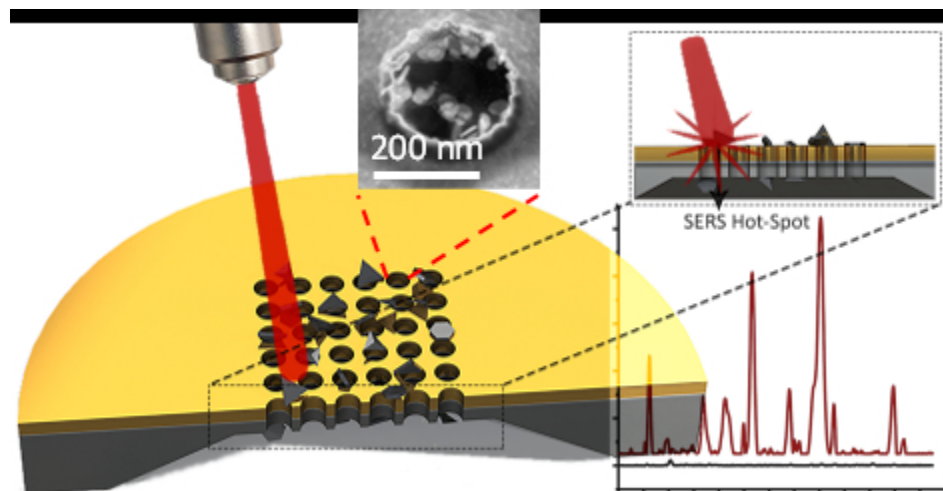
COMMUNICATION

Figure SI 11. R6G Raman spectra obtained at the NHAs, while under 2.0 applied potentials with various instrumental settings, where the laser power used is, (a) $4\ mV$, (b) $7\ mV$, (c) $10.5\ mV$, (d) $15.7\ mV$, and (e) $23.4\ mV$, exposed for $1\ s$, $3\ s$, $5\ s$, $8\ s$, $10\ s$ of integration time.

Reference

1.   F. Adar, *Spectroscopy*, 2010, **25**, 23.

80x41mm (150 x 150 DPI)